Elevated Potential Instability in the Comma Head: Distribution and Development

ANDREW A. ROSENOW

Department of Atmospheric Sciences, University of Illinois at Urbana–Champaign, Urbana, Illinois, and Cooperative Institute for Mesoscale Meteorological Studies, University of Oklahoma, and NOAA/OAR National Severe Storms Laboratory, Norman, Oklahoma

ROBERT M. RAUBER, BRIAN F. JEWETT, GREG M. MCFARQUHAR,[a] AND JASON M. KEELER[b]

Department of Atmospheric Sciences, University of Illinois at Urbana–Champaign, Urbana, Illinois

(Manuscript received 29 September 2017, in final form 2 March 2018)

ABSTRACT

The development of elevated potential instability within the comma head of a continental winter cyclone over the north-central United States is examined using a 63-h Weather Research and Forecasting (WRF) Model simulation. The simulation is first compared to the observed cyclone. The distribution of most unstable convective available potential energy (MUCAPE) within the comma head is then analyzed. The region with positive MUCAPE was based from 2- to 4-km altitude with MUCAPE values up to 93 J kg^{-1}. Backward trajectories from five sublayers within the region of elevated convection in the comma head were calculated to investigate how elevated potential instability developed. Air in the lowest sublayer, the source air for convective cells, originated 63 h earlier near Baja California at elevations between 2.25- and 2.75-km altitude. Air atop the layer where convection occurred originated at altitudes between 9.25 and 9.75 km in the Arctic, 5000 km away from the origin of air in the lowest sublayer. All air in the layer in which convection occurred originated over the Pacific coast of Mexico, the Pacific Ocean, or arctic regions of Canada. Diabatic processes strongly influenced air properties during transit to the comma head. Air underwent radiative cooling, was affected by mixing during passage over mountains, and underwent interactions with clouds and precipitation. Notably, no trajectory followed an isentropic surface during the transit. The changes in thermodynamic properties along the trajectories led to an arrangement of air masses in the comma head that promoted the development of potential instability and elevated convection.

1. Introduction

The comma head region of wintertime extratropical cyclones is frequently the source of extreme winter weather, including heavy snow and ice storms. Elevated convection, sometimes associated with wintertime lightning, has been shown to form over a stable layer within the comma head of winter cyclones (e.g., Martin 1998; Halcomb and Market 2003; Moore et al. 2005; Rauber et al. 2014; Warner et al. 2014). Most reports involve thunderstorms forming above a stable layer capped by a frontal surface. About 53% of all thundersnow reports in the United States were associated with continental cyclones (Rauber et al. 2014). Climatological studies by Curran and Pearson (1971), Colman (1990), Holle and Cortinas (1998), and Market et al. (2002) have indicated that wintertime elevated thunderstorms are most common across the central plains of the United States.

Elevated convection within the comma head of winter cyclones over the continental United States manifests in two modes: cloud-top generating cells and deeper convective cells emerging from above a frontal surface and rising toward the tropopause (Rauber et al. 2014; Rosenow et al. 2014). Cloud-top generating cells appear locally at the top of otherwise stratiform clouds and produce streamers of precipitation that descend into the stratiform layer. Comprehensive reviews related to generating cells and their role in precipitation processes

[a] Current affiliation: Cooperative Institute for Mesoscale Meteorological Studies, and School of Meteorology, University of Oklahoma, Norman, Oklahoma.

[b] Current affiliation: Department of Earth and Atmospheric Sciences, University of Nebraska–Lincoln, Lincoln, Nebraska.

Corresponding author: Andrew A. Rosenow, andrew.rosenow@noaa.gov

DOI: 10.1175/MWR-D-17-0283.1

within the comma head appear in Rosenow et al. (2014), Kumjian et al. (2014), Rauber et al. (2014, 2015), Plummer et al. (2014, 2015), and Keeler et al. (2016a,b, 2017). Modeling studies by Keeler et al. (2016b, 2017) show that the primary forcing for generating cells is radiative cooling. The generating cells' intensity and organization was shown to be controlled by the stability of the environment in which they form, whether or not solar shortwave radiative warming is present to offset cloud-top longwave radiative cooling, and the vertical shear across the altitudes at which they occur.

The source of instability for the second mode of elevated convection within the comma head, deep elevated convective cells, is less well understood. Direct observation of deeper emergent convective cells comes primarily from vertically pointing short-wavelength radars and studies of wintertime lightning [see review in Rauber et al. (2014)]. As noted by Rauber et al. (2014), evidence from past studies suggests that stability varies across the comma head of cyclones, from a potentially unstable environment on the equatorward side to a stable environment on the poleward side, with very limited evidence for moist symmetric instability (Wiesmueller and Zubrick 1998; Martin 1998; Nicosia and Grumm 1999; Novak et al. 2008, 2009). Novak et al. (2010), for example, found that when the comma head region of east coast cyclones is characterized by a single dominant precipitation band, the band forms as frontogenesis increases and elevated stability is reduced, and it dissipates as frontolysis occurs. In their study, elevated instability most often occurred during the early period of band formation, suggesting that the atmosphere in the banded region stabilized with time, due in part to the redistribution of moisture and latent heat associated with the band circulations. Observations presented by Rauber et al. (2014), Rosenow et al. (2014), Murphy et al. (2017), Grim et al. (2007), and Han et al. (2007) provide evidence that potential instability develops on the equatorward side of the comma head as an upper-tropospheric dry air layer intrudes into the comma head region over a moist stable cloud layer. Wexler and Atlas (1959) first hypothesized that this dry air aloft might have upper-tropospheric (and lower stratospheric) origin and arrive behind the cyclone's upper-level front (Reed and Sanders 1953; Reed 1955). Studies in the United Kingdom have shown that tropopause folds and the associated dry air intrusion produced instability within the warm conveyor belt and low-pressure center (e.g., Browning and Golding 1995; Griffiths et al. 2000).

During the Profiling of Winter Storms (PLOWS) experiment (Rauber et al. 2014), this overrunning layer of dry air, in some cyclones, was potentially unstable, and deep elevated convective cells were observed to rise from just above the frontal interface, through the dry air mass, and to the tropopause. This can be seen in Fig. 1, where convective echoes dominate the southern (right) half of the radar cross section (see also Rauber et al. 2014; Rosenow et al. 2014; Murphy et al. 2017). On the 0.5° scan of WSR-88Ds, this zone appears as a region of cellular echoes [see Fig. 5 of Rosenow et al. (2014)]. The updrafts within these cells were found to be on the order of 1–5 $m\,s^{-1}$ (Rosenow et al. 2014), wintertime lightning discharges (e.g., Market et al. 2002, 2006) were common (Rauber et al. 2014; Warner et al. 2014), and the microphysical properties of the cells supported conditions for inductive charging (Rauber et al. 2014; Murphy et al. 2017). However, the processes by which air within the comma head is organized to create potential instability and, thus, enable the generation of elevated convection have yet to be adequately explained.

The purpose of this paper is to quantitatively define the source of instability associated with the deeper convective cells that emerge from above the frontal surface and rise toward the tropopause within the comma head, with the purpose of providing increased understanding of how potential instability develops in the comma head of continental winter cyclones. The results of a numerical simulation of the cyclone that occurred on 8–9 December 2009 (Rauber et al. 2014; Rosenow et al. 2014; Murphy et al. 2017) are presented to explore how the environment for elevated convection develops. Trajectory analysis is used to quantify how air parcels approaching the comma head from various source regions are modified along their trajectories by diabatic processes and subsequently stack vertically, such that they arrive in the comma head in a configuration where elevated instability exists and can be released in the form of elevated convection. The 8–9 December 2009 storm was chosen for the simulation because it had well-documented elevated convection that produced occasional lightning discharges and was associated with positive most unstable convective available potential energy (MUCAPE) above the frontal inversion, making it the best case from the PLOWS dataset for this analysis. The first goal was to produce a simulation of the cyclone that was consistent structurally with the observed cyclone, particularly in that it produced the observed instability in the southern sector of the comma head. Trajectory analyses are then used to understand the Lagrangian thermodynamic evolution of air that results in the creation of the layer in which convection forms. A number of studies have used trajectories to examine airflows in cyclones, but these studies have generally focused on larger-scale features, such as conveyor belts (e.g., Schultz and Mass 1993; Wernli and Davies 1997; Pfahl et al. 2014; Rasp et al. 2016).

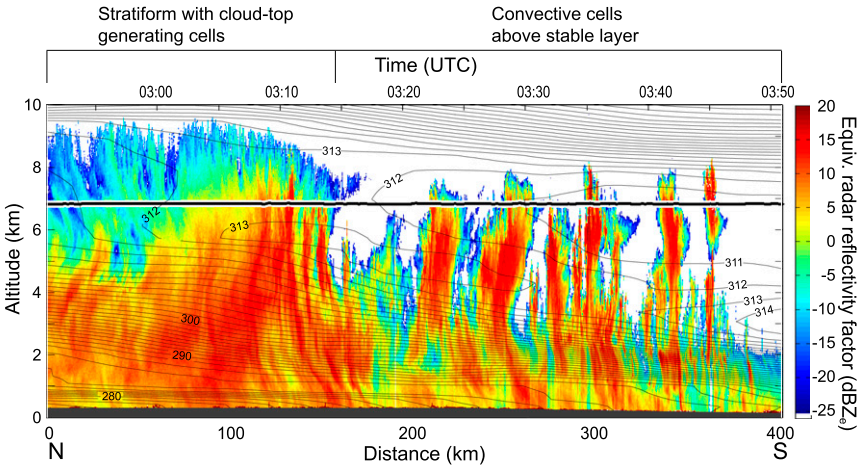

FIG. 1. WCR W-band equivalent radar reflectivity factor overlaid with RUC contours of θ_e at 0300 UTC 9 Dec 2009 [Adapted from Rosenow et al. (2014); the location of the cross section is given in Fig. 3]. Labels above the image indicate the locations of the regions stratiform (north) and elevated convective (south) dominated precipitation.

The remainder of the paper is organized as follows. The numerical simulation and analysis methodology is described in section 2. Section 3 presents a comparison of the simulation with the observations. Section 4 presents an analysis of potential instability in the comma head in both the observations and simulation. Section 5 uses trajectory analysis to investigate the development of the elevated instability within the modeled cyclone, and section 6 presents the same analysis for an observed convective cell. Section 7 presents a discussion of the results, and section 8 presents a summary of the findings.

2. Methodology

This study uses observations from PLOWS, initialization data from 13-km Rapid Update Cycle (RUC) model analyses (Benjamin et al. 2004), and results from a numerical simulation of the Weather Research and Forecasting (WRF) Model configured to study elevated instability and convection within the cyclone comma head. Data presented herein are from special rawinsondes and equivalent radar reflectivity factor (hereafter reflectivity) measurements from the W-Band Wyoming Cloud Radar (WCR) on board the National Science Foundation/National Center for Atmospheric Research (NSF/NCAR) C-130 aircraft. PLOWS deployment strategies and WCR data-processing routines are described in Rosenow et al. (2014), Rauber et al. (2014), and Plummer et al. (2014).

A simulation of the 8–9 December cyclone was carried out using the WRF Model, version 3.5.1 (Skamarock et al. 2008). Two domains were used with horizontal grid spacing of 9 km (1002 × 714 grid points) and 3 km (988 × 907 points), respectively (Fig. 2). The model was configured with 120 vertical levels, focused on the troposphere, with a model top of 60 hPa. The model resolution and domain were chosen to allow trajectories to remain within the domain and to ensure that mesoscale flow features, particularly around fronts, were sufficiently resolved to allow the formation of potential instability. Global Forecast System (GFS) model data were used for model initialization and 6-hourly boundary conditions. Experiments with alternative advection schemes, different parameterizations, resolution and time step changes, and nudging were carried out as part of this study, with the goal of simulating a cyclone that, as closely as possible, matched the actual storm structure, particularly the development of potential

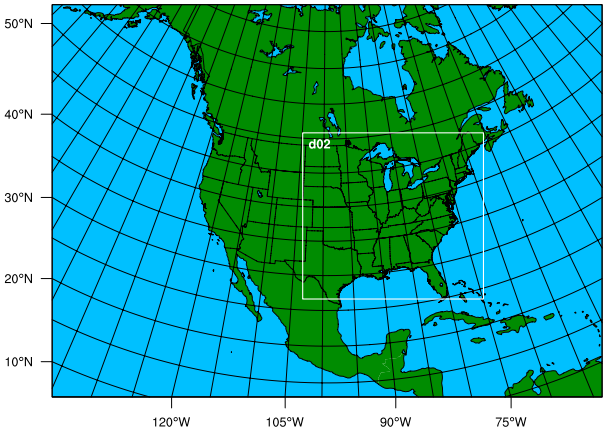

FIG. 2. Domains used in the simulation. The entire map represents the size of the outer domain, and the white box represents the size of the nested domain.

TABLE 1. Nondefault WRF settings used for the simulation

WRF parameter	Setting(s)
Run time	3 days, 18 h
Initialization time	1200 UTC 6 Dec 2009
History output interval	5 min
Time step (outer domain)	20 s
No. of domains	2
nx, *ny*	Domain 1: 1 002 712; domain 2: 988 907
Vertical levels	120
dx, *dy*	Domain 1: 9 km; domain 2: 3 km
Domain *x*, *y* start	457, 179
Microphysics option	8 (Thompson microphysics)
Radiation LW/SW physics	4 (RRTMG scheme)
Radiation *dt*	5 min
sf_sfclay, sf_surface physics	1, 2 (Monin–Obukhov, Noah LSM)
Boundary layer scheme, *dt*	1 (YSU scheme), every time step (0)
cu_physics, cudt (cumulus parameterization, *dt*)	Domain 1: 1 (Kain–Fritsch), 5 min; domain 2: 0 (no cumulus parameterization)
damp_opt (damping)	3 (gravity wave damping layer)
Zdamp	5000 m
epssm	0.5
Horizontal, vertical advection order	Fifth order
Time step for sound	6 s
Moist, scalar advection	4 (fifth-order WENO)

instability within the comma head region. The simulation presented herein is the one that most closely represented the actual storm in terms of position, intensity, and precipitation distribution. The settings and parameterizations used for the WRF simulation appear in Table 1 and are summarized below.

The Kain–Fritsch cumulus parameterization (Kain and Fritsch 1990) was used for the outer domain. The inner domain was convective permitting. The model time step was 20 s in the outer domain and 6.67 s in the inner domain. Thompson microphysics (Thompson et al. 2008) and Rapid Radiative Transfer Model for Global Climate Models (RRTMG; Iacono et al. 2000) radiation schemes were used based on favorable comparisons to PLOWS observations in testing described by Keeler et al. (2016a). A 5-km-deep gravity wave damping layer (Klemp et al. 2008) was placed at the top of the model to prevent wave reflection off the model top.

The model initialization time was chosen to be 63 h (60 h plus 3 h to allow model initialization at the nearest synoptic time) prior to the time of the intensive observation period with the WCR (Fig. 1). Output was saved every 5 min to provide high temporal resolution data for computation of trajectories.

Trajectory release points were selected based on the presence and location of potential instability in the model. Back trajectories were calculated from points along model cross sections comparable to the observed radar cross section (Fig. 3) so that the trajectories provide information about the sources of air in which potential instability developed. A representative portion of the calculated trajectories are presented here. Trajectories were calculated on the 9-km domain. However, two-way nesting allowed circulations on the convective scale simulated in the inner 3-km domain to be represented in the trajectory calculations. The Read–Interpolate–Plot (RIP) software package was used to calculate backward trajectories (Stoelinga 2009; Sippel et al. 2011; Schumacher and Johnson 2008).

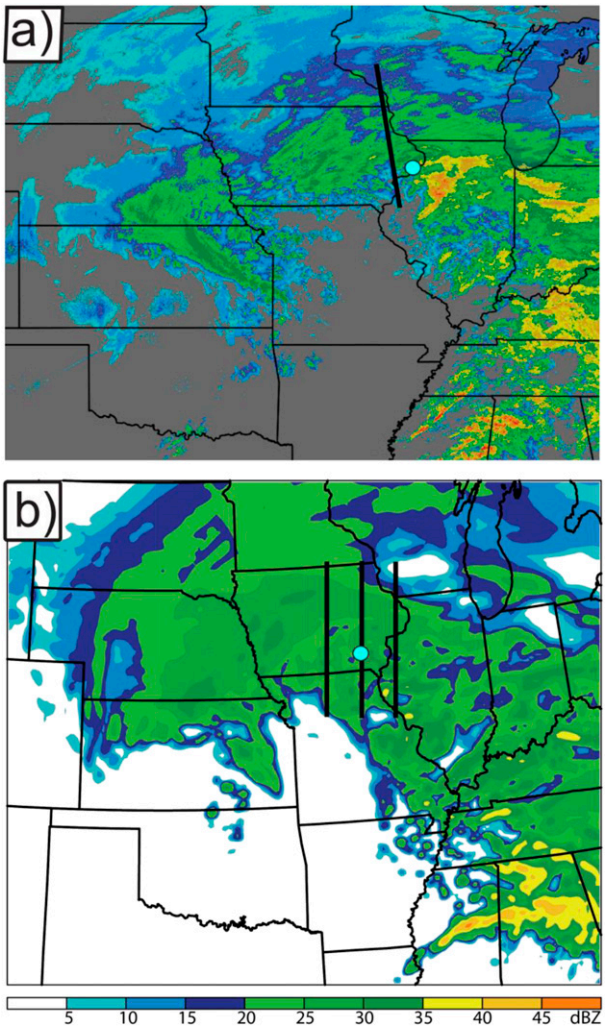

FIG. 3. (a) WSR-88D composite valid at 0305 UTC 9 Dec 2009. Black line indicates the flight leg where the radar data in Fig. 1 were collected. Cyan dot indicates sounding location in Fig. 8a. (b) WRF simulated radar reflectivity (colors) valid at 0300 UTC 9 Dec 2009. Black lines indicate location of model cross sections where back trajectories were released. Cyan dot indicates sounding location in Fig. 8b.

Values of potential temperature θ, equivalent potential temperature θ_e, and mixing ratio q, which are conserved variables for adiabatic and/or pseudoadiabatic flow, as well as other variables, such as temperature, were saved along trajectories. Changes in conservative parameters along trajectories illustrate the nature of diabatic and mixing processes that occur as air moves toward the comma head.

3. Comparison of simulation with analysis

This section compares the synoptic-scale structure of the observed cyclone with the WRF simulation at two times, 48 and 60 h after model initialization. Figure 4 shows six panels: two each at 300 hPa, 500 hPa, and the surface, and all valid at 1200 UTC 8 December 2009. Analyses in the left column are from the initialization of the RUC model (hereafter, the analysis), and the right column, 48-h forecasts from the WRF Model (hereafter, the simulation).

The 8–9 December 2009 cyclone formed near 1200 UTC 8 December as a short-wave trough with an associated ~70 m s^{-1} jet streak moved across the Rocky Mountains (Fig. 4a). While the jet stream position appears qualitatively similar between the analysis and simulation, subtle variations led to differences in cyclone evolution in the simulation, compared to the observations. The jet stream axis at 300 hPa in the simulation (Fig. 4b) was about 150 km farther north than in the analysis, which resulted in a shift of the left exit region of the jet streak a similar distance northward. The jet streak also was slightly stronger in the simulation, with the area of winds in excess of 70 m s^{-1} larger than in the analysis.

The axis of the vorticity maximum at 500 hPa associated with the short-wave trough was located over central and northern Arizona at 1200 UTC in the analysis (Fig. 4c), placing the ascent region associated with differential cyclonic vorticity advection over northern New Mexico. The vorticity maximum in the simulation was about 100 km farther north of its position in the analysis at 500 hPa, compared to the simulation (Fig. 4d). In addition to the position difference, the vorticity maximum extended to the north by an additional 100 km, which led to increased ascent to the north of the region of maximum ascent in the analysis.

At the surface in the analysis, the cyclone first formed in north-central New Mexico within a surface trough of low pressure (Fig. 4e). The trough, with minimum pressure around 990 hPa, extended south from a deeper 984-hPa cyclonic circulation in western Colorado. The developing cyclone over New Mexico moved east in the next 12 h to become the mature cyclone over the plains, while the low pressure center over Colorado weakened. In the simulation (Fig. 4f), the cyclone over western Colorado was also present with a slightly higher minimum pressure (986 hPa). However, the pressure trough to the southeast over New Mexico was notably absent. In the simulation, the low pressure center in Colorado moved east to become the cyclone over the plains during the next 12 h.

Figure 5 shows a six-panel plot of the same fields as Fig. 4, but for 0000 UTC 9 December, 3 h before the cross-sectional analysis presented in the next section. In the analysis, by 0000 UTC, the jet streak had expanded and progressed east, now consisting of multiple speed maxima. The left exit region of the 70 m s^{-1} lead speed maximum was located over southwest Missouri and southeast Kansas (Fig. 5a). At 300 hPa in the simulation (Fig. 5b), the easternmost end of the 70 m s^{-1} jet streak over northwest Arkansas and northeast Oklahoma was about 50 km farther northwest than in the analysis, which shifted the left exit region a similar distance northwest compared to the analysis.

At 500 hPa, the vorticity maximum associated with the short-wave trough in the analysis progressed to the east-northeast and was centered over Kansas and Oklahoma (Fig. 5c). The 500-hPa vorticity pattern in the simulation (Fig. 5d) had the vorticity maximum 50–100 km farther west with a more negative tilt.

At the surface, the cyclone had a minimum pressure of 995 hPa over southern Missouri in the analysis (Fig. 5e), but would eventually deepen to around 980 hPa over southern Lake Michigan by 1200 UTC 9 December (not shown). At the surface in the simulation (Fig. 5f), the cyclone was both deeper (984 hPa) and ~300 km farther west when compared to the analysis at 0000 UTC. This difference continued to be evident at 0300 UTC (Fig. 6), as the analyzed cyclone had a minimum mean sea level pressure of 991 hPa, and the simulated cyclone had a minimum pressure of 983 hPa.

As the observed cyclone matured, it produced a large precipitation shield, as evidenced by the 0005 UTC 9 December radar composite in Fig. 6a. The cyclone produced precipitation across an extensive area of the United States, from deep within the warm sector in the southeastern United States back across the comma head, which was located from Kansas to Wisconsin and Illinois. In the comma head region, there was extensive precipitation, mostly heavy snow, across much of Iowa, Minnesota, Wisconsin, Kansas, and Illinois. Stratiform, banded precipitation was observed on the poleward side of the comma head, while in the southern and eastern portions (the equatorward side) of the comma head, more cellular echoes were present associated with the elevated convection [see Fig. 5 of Rosenow et al.

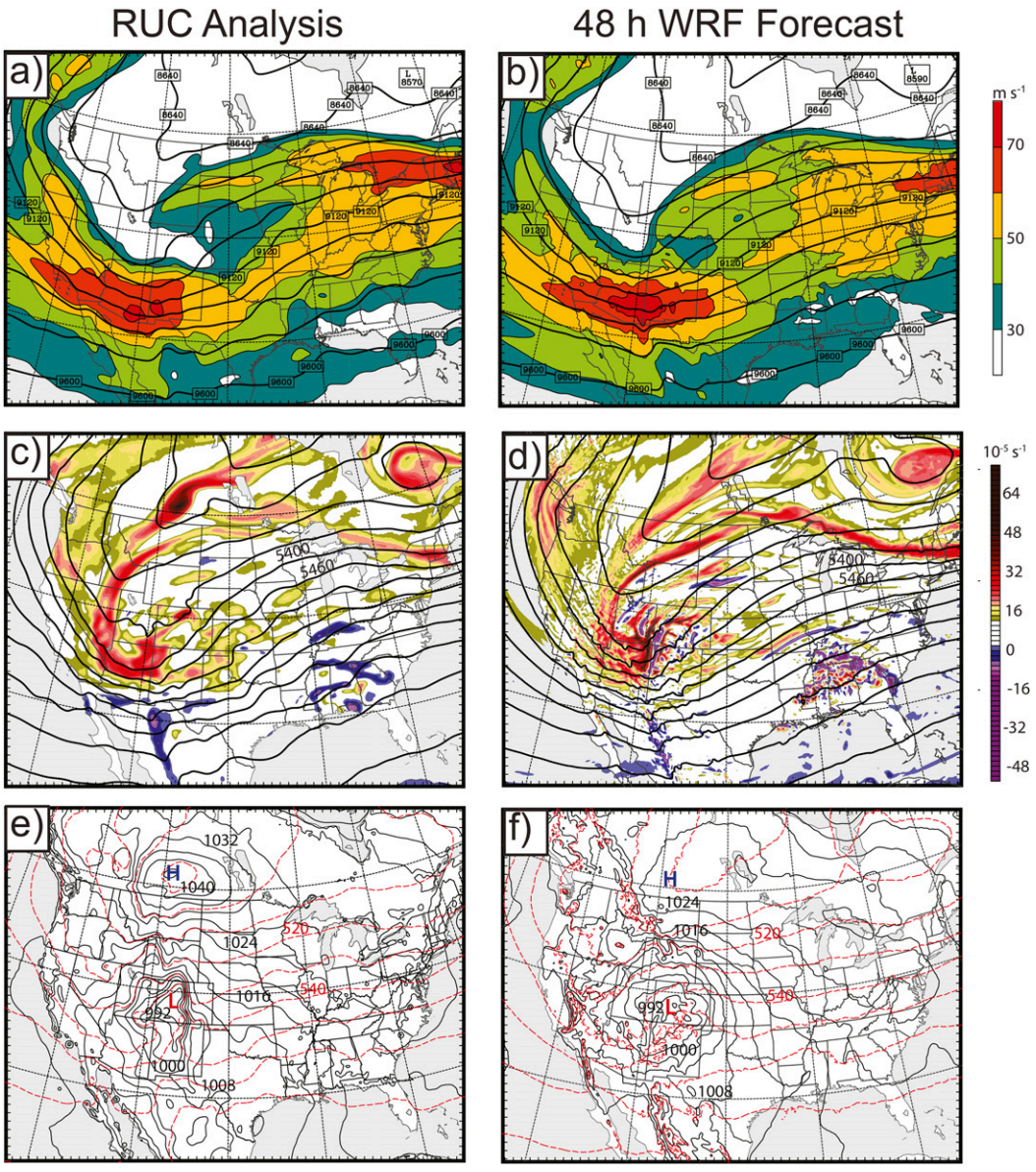

FIG. 4. Analyses valid at 1200 UTC 8 Dec 2009 from (a),(c),(e) the RUC initialization and (b),(d),(f) the WRF simulation. (a),(b) 300-hPa heights (contours, m) and winds (colors, m s^{-1}); (c),(d) 500-hPa heights (contours, m) and absolute vorticity (colors,10^{-5} s^{-1}); and (e),(f) mean sea level pressure (solid contours, hPa) and 1000–500-hPa thickness (red dashed contours, dam).

(2014)]. The corresponding 1 km above mean sea level radar reflectivity associated with the simulated cyclone is shown in Fig. 6b. When compared to the observed radar reflectivity in Fig. 6a, the WRF reflectivity resembles the reflectivity composite when the shift in the cyclone center westward in the simulation is taken into account. The model captured the extensive warm-sector precipitation, the large, stratiform echoes in most of the comma head, and the more cellular precipitation on the southern and eastern edge of the comma head.

Overall, the simulated cyclone was structurally similar on the large scale, but the center of the simulated cyclone was approximately 300 km west when compared to the analysis. As noted in section 2, several additional simulations were carried out in an attempt to simulate a storm that more closely matched the observed cyclone in evolution and location. The simulation shown was the one that most closely represented the actual storm. Additionally, features above the surface differ less between the

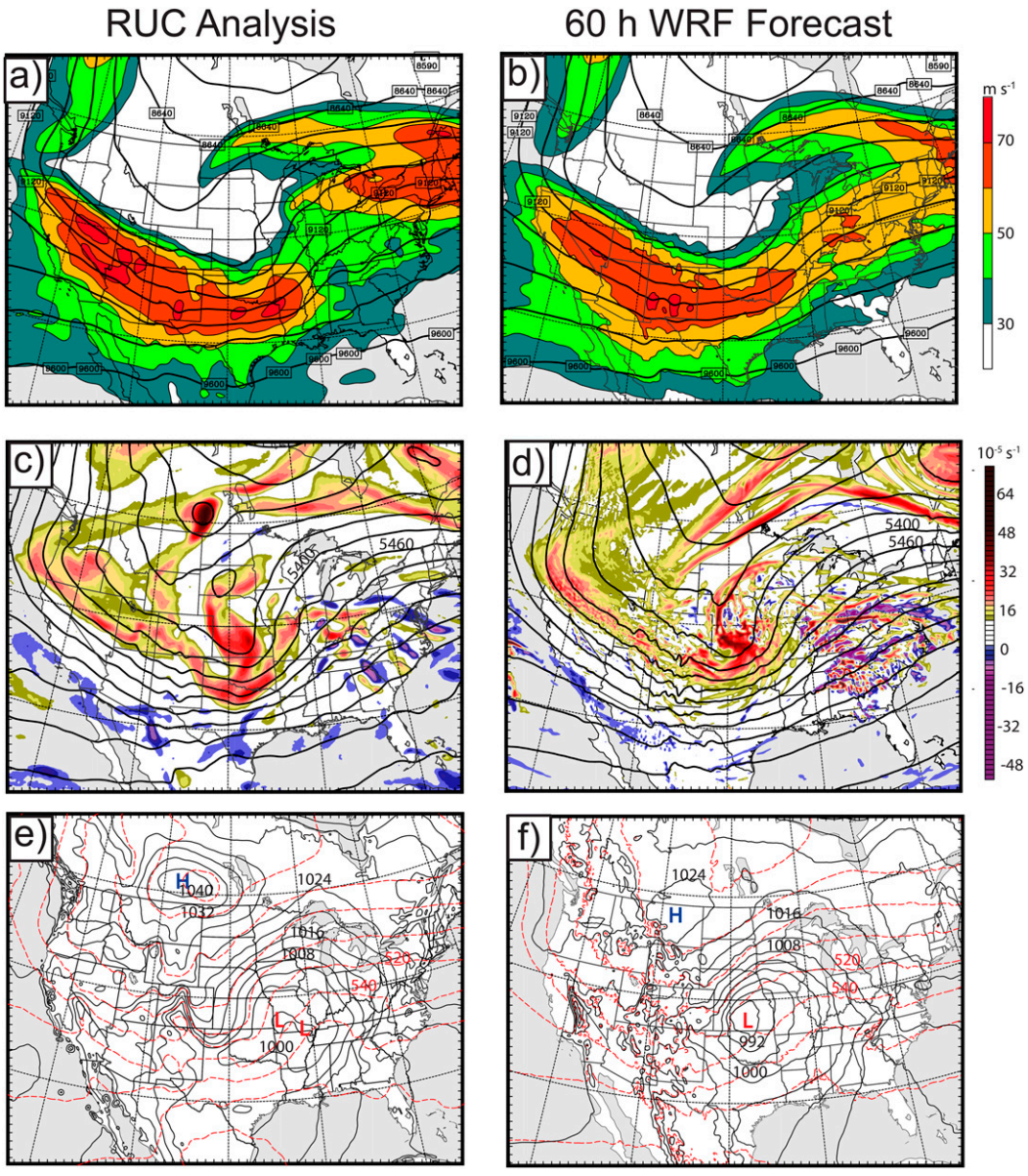

FIG. 5. As in Fig. 4, but for 0000 UTC 9 Dec 2009.

simulation and observations, even down to 850 hPa (not shown).

This study focuses on the development of elevated instability and air parcel trajectories into the region of elevated instability. The importance of the elevated instability and antecedent airflows that produce that instability comes from their position relative to the cyclone, not relative to geography. Additionally, as will be shown in subsequent sections, trajectories from the elevated potentially unstable region do not travel near the surface in the vicinity of the cyclone. The position errors of the surface cyclone, as will become apparent, were not critical to addressing the questions regarding the generation of instability.

4. Convection and potential instability

Figure 7a shows the WCR reflectivity overlaid with θ_e from the RUC analysis at 0300 UTC 9 December. Elevated convective cells are present, extending to near the tropopause from the top of the stable layer at 3–5-km altitude. These cells' environment was potentially unstable, with θ_e values reaching a local maximum of 313–314 K just above the frontal boundary, decreasing

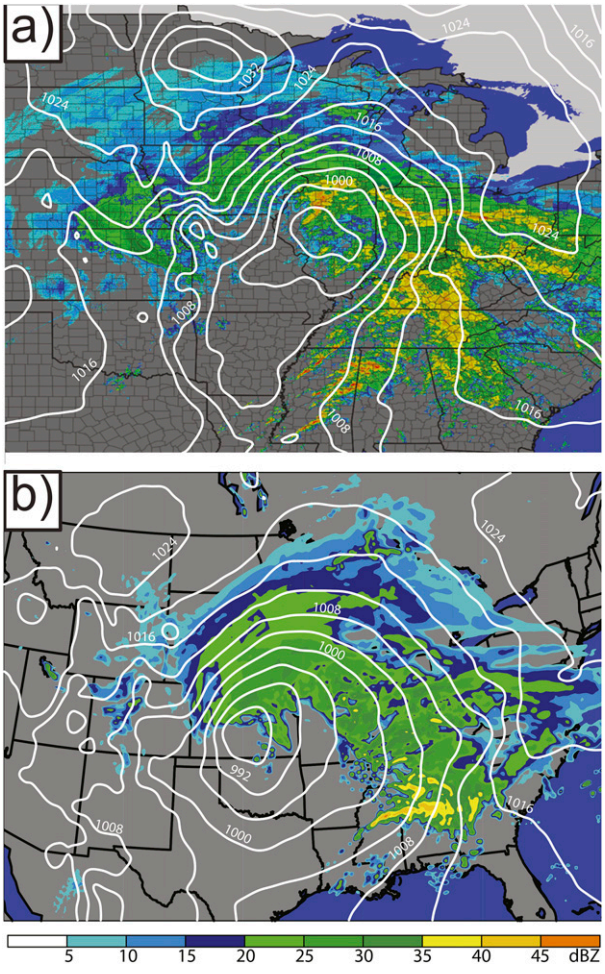

FIG. 6. (a) WSR-88D reflectivity composite for 0005 UTC 9 Dec 2009 overlaid with 0000 UTC 9 Dec RUC initialization mean sea level pressure contours. (b) Simulated radar reflectivity valid at 0000 UTC 9 Dec 2009 overlaid with simulated mean sea level pressure.

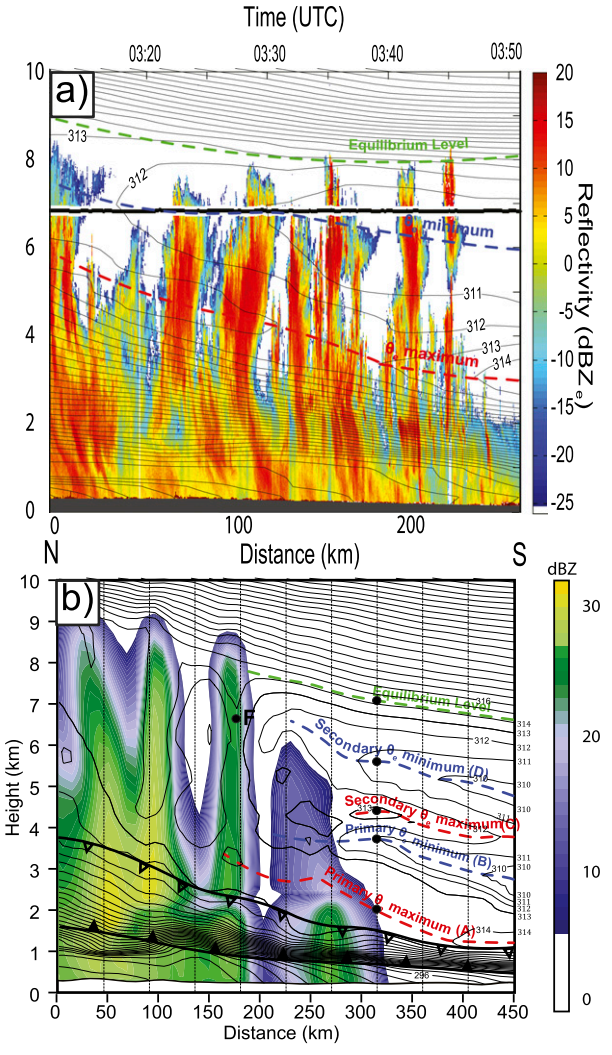

FIG. 7. (a) WCR reflectivity and RUC θ_e from a cross section of the 9 Dec cyclone indicated in Fig. 1. The black horizontal line is the flight track. Adapted from Rosenow et al. (2014). (b) Simulated radar reflectivity (colors) and θ_e (contours) from the easternmost cross section in Fig. 3 at 0300 UTC 9 Dec. Dashed colored lines on both panels indicate distinct layers in the convective region; letters in parentheses indicate layer name used throughout the paper. Black dots at $x = 325$ km indicate trajectory locations in Fig. 11. Black dot labeled "F" is for the trajectory in Fig. 13. Note difference in horizontal scale between the top and bottom panels. Different color scales are used for reflectivity, since (a) represents reflectivity measured by a W-band radar, while (b) represents simulated S-band reflectivity.

to 311–312 K in the 6–7-km range, which was a local minimum in θ_e, and then increasing again to the equilibrium level at the tropopause, with saturated air (with respect to ice) present within the potentially unstable layer. The instability of the environment in the convective region of the comma head of the cyclone was also evident from soundings taken during the storm (e.g., Fig. 8a). An example sounding, which was launched near convective cells at 0400 UTC 9 December (see location in Fig. 3a), had 241 J kg^{-1} of MUCAPE. Four other soundings launched from the same location between 0000 and 0800 UTC had positive MUCAPE values (Rauber et al. 2014). The observations of MUCAPE, combined with radar observations of convection, directly confirm the presence of elevated instability in the environment where the convective cells were observed. While MUCAPE is a measure of conditional instability rather than potential instability (Schultz and Schumacher 1999) because the air is saturated and therefore $\overline{\theta}_e^* = \overline{\theta}_e$ (see Schultz and Schumacher 1999, their Table 1), it is presented as a representation of the magnitude of instability. Rosenow et al. (2014), Rauber et al. (2014), and Murphy et al. (2017) have previously demonstrated that the cells observed in the 8–9 December

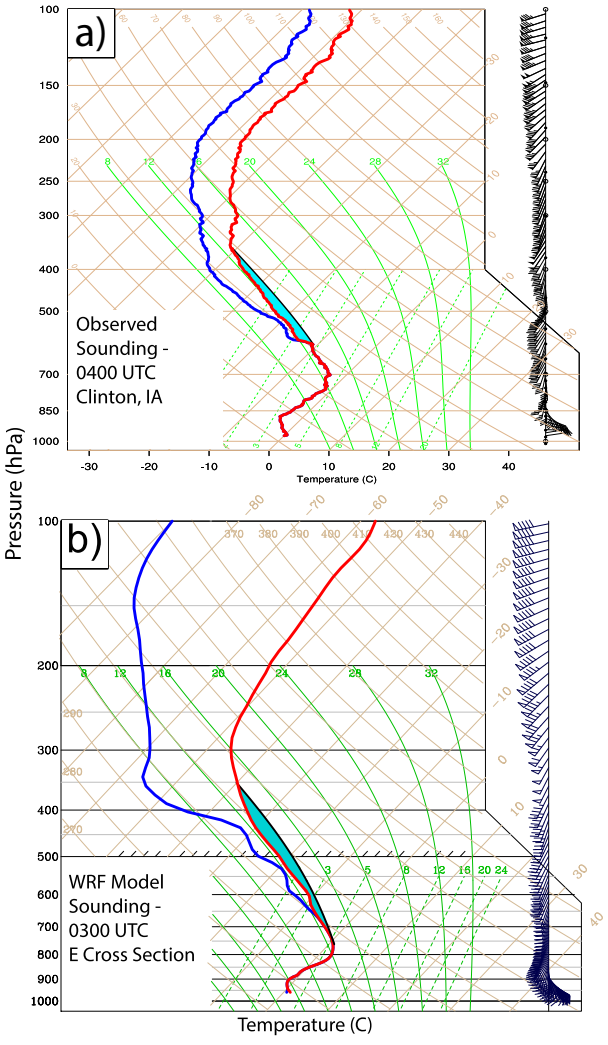

FIG. 8. Observed 0400 UTC special sounding taken from Clinton, IA (cyan dot in Fig. 3a), in the convective region of the cyclone on 9 Dec 2009. (b) WRF Model sounding from within the convective region of the cyclone at the point indicated in Fig. 3b at 0300 UTC 9 Dec 2009. Red lines are temperature, blue lines are dewpoint temperature, black lines indicate most unstable parcel paths, cyan fill indicates positive area (buoyancy) for most unstable parcels, and winds are in m s^{-1} with a full barb and a flag representing 5 and 25 m s^{-1}, respectively.

cyclone have expected characteristics of elevated convection, including vertical velocities between 1 and 7 m s^{-1}, as well as graupel, charging, and occasional lightning.

Figure 7b shows a cross section of reflectivity and θ_e contoured at every 0.5 K from the simulation across the convective region. The vertical cross section in Fig. 7a can be compared with the simulated reflectivity and θ_e distribution at 63 h into the simulation in Fig. 7b to confirm that the simulation produced a comparable representation of the environment of the elevated convective region (e.g., presence of instability, depth of unstable layer, presence of convective cells, and similar θ_e distribution). As with the convection observed with the WCR, simulated convective echoes extend from the top of the stable layer at 2–3 km to the tropopause at 8–9 km. These narrow, tall echoes are convective, as they are located in the inner 3-km grid with no cumulus parameterization, and coincide with updrafts of 1–2 m s^{-1} in the model (also discussed later in section 6). The maximum updrafts in the simulation were smaller in magnitude than those in the observations (Rosenow et al. 2014), an expected outcome of the horizontal grid spacing of the simulation (3 km). The convective cells in the simulation developed in a potentially unstable environment, as is evident in the θ_e distribution. The θ_e values reach a local maximum of ~314 K just above the top of the stable layer, which extends from 3- to 1.5-km altitude (from 150 to 450 km along the cross section horizontally). The values of θ_e decrease to a local minimum of 310–312 K in the 6–7-km range, similar to the analysis. The equilibrium level for parcels originating at the θ_e maximum is at the tropopause, which is located between 7 and 9 km, increasing in altitude from south to north.

The potential instability present in the simulation can be seen in model soundings, an example of which is shown in Fig. 8b. While the MUCAPE in this sounding is not as pronounced as in the observed sounding, there is still a clear layer of instability based at around 640 hPa up to an equilibrium level near the tropopause at around 350 hPa, a layer of similar depth when compared to the analysis in Fig. 8a. The instability is based above the stable layer.

The air above the elevated frontal boundary in the simulation consists of distinct layers (Fig. 7b). These layers were present in other cross sections from the simulated storm taken ~100 km apart in space and 2 h apart in time (Fig. 3b). The first layer, layer A, lies above the surface-based stable layer and represents warmer, moister air, characterized by a maximum in θ_e. This layer slants upward from 1.5-km altitude in the south at x = 450 km in Fig. 7b to about 5 km in the north at x = 150 km. The value of the θ_e maximum, with magnitudes around 313–314 K, is consistent with the analysis (Fig. 7a). It is this air that ascends in convection in the simulation, as will be demonstrated in the next section.

Layer B, marking a primary θ_e minimum, lies above layer A. The axis of the θ_e minimum slants upward from about 2.75-km altitude in the south to about 4 km in the middle of the cross section in Fig. 7b. The θ_e values within this layer ranged from 310 K in the south to 312 K in the north, similar to the minimum in the analysis in Fig. 7a. Unlike the analysis, there are two additional

sublayers in the simulation. Layer C, a secondary maximum above layer B, extended from about 3.75 km in the south to 4.25 km in the middle of the cross section. At the time of the cross section, the secondary maximum in θ_e had smaller values than the primary maximum in layer A, with the secondary maximum having magnitudes of 312–313 K. Above this secondary maximum was a secondary minimum, layer D, with its axis extending from an altitude of ~4.75 km in the south to ~7 km in the middle of the cross section. Finally, the equilibrium level (layer E) was located from ~7- to ~8-km altitude, similar to the analysis in Fig. 7a. Within layer E, θ_e values were the same value as in layer A, approximately 314 K.

In addition to the aforementioned layers, a convective cell was present at about $x = 150$ km in Fig. 7b. The effect of this cell on the background θ_e fields stands out. Instead of decreasing with height, θ_e is nearly constant with height within the cell due to upward transport of potentially warm air within the convection. Remnants of a second cell appear farther to the north. The tall, cellular echoes reach the equilibrium level, with more stratiform echoes present in the stable air between the ground and layer A, qualitatively similar to cells observed with the WCR (Fig. 7a). The convective cells and associated trajectories will be examined in more detail in section 5.

The region of elevated potential instability evolved in both location and magnitude within the cyclone in the simulation. Figure 9a shows a plan view of the maximum MUCAPE from the simulation, valid at 0100 UTC 9 December 2009. The solid black lines are the 10-dBZ contours of reflectivity from the simulation at the same time. Figure 9b shows the lifting condensation level (LCL) of the parcel with the maximum MUCAPE value indicated in Fig. 9a. For the elevated convection in the comma head, which originates at the top of the surface-based stable layer within saturated air, as shown in the sounding in Fig. 8b, the LCL corresponds to the level of free convection (LFC). At 0100 UTC, precipitation was located across Illinois, Missouri, and Indiana, and the model indicated potential instability coincident with this precipitation in the southern part of the comma head (Figs. 9a,b), with MUCAPE values around 50 J kg^{-1} in northeast Missouri. The MUCAPE across northern Missouri, southern Iowa, and central Illinois was based in the 2.5–4.5-km range, which is consistent with the altitude of layer A in Fig. 7b.

By 0300 UTC 9 December, the MUCAPE across southern Iowa increased, with the maximum in MUCAPE reaching 93 J kg^{-1} (Fig. 9c). The increase in potential instability occurred within the precipitation region on the south side of the comma head, as indicated by the 10-dBZ contour in Fig. 9c. Figure 9d shows that the instability is once again elevated, with parcels with MUCAPE values having LCLs generally in the 3–4-km range across southern Iowa and central Illinois, consistent with the altitude of layer A in Fig. 7b and the sounding in Fig. 8b.

5. Trajectory analysis

Backward trajectories were calculated to establish the history of air in the layer in which elevated convection occurred within the comma head. The goal of this analysis is to understand the thermodynamic changes that led to the preconvective environment that supported elevated convection in the comma head. Trajectories shown here are from each of the layers indicated in Fig. 7b.

Trajectories were initialized in three north–south-oriented two-dimensional y–z planes across the simulated comma head region at 0100 UTC, prior to widespread elevated convective development in the simulation's comma head, and at 0300 UTC, after the elevated convection developed. The cross sections were chosen based on the location of the region of maximum elevated MUCAPE in the comma head within the simulated storm (Fig. 9c). Trajectories were released within these vertical planes at points within layers A–E at these two times at every 9 km in the y direction and every 0.25 km in altitude above the boundary layer. Example trajectories will be shown herein to demonstrate the evolution of air arriving within the layer in which convection occurred within the comma head.

The trajectories arriving within each of the layers (A–E) had similar source regions at both times presented here, as well as other surrounding times, which are not shown for the sake of brevity. The source points for trajectories arriving in each layer appear in Fig. 10. The trajectories are plotted for points 45 km apart in the north–south direction along each layer.

In Fig. 10a, the source points are for trajectories released from the eastern cross section in Fig. 3b at 0300 UTC. Air arriving in layer A originated over the eastern Pacific near Baja California (region A in Fig. 10a), with the exception of one location over north-central Mexico, and the air originated at altitudes from 2.25- to 2.75-km altitude (not shown). Layer B air originated in region B in Fig. 10a between 2.2- and 3-km altitude, to the northwest of region A. Layer C was smaller in horizontal extent, so there were fewer trajectories. These trajectories originated at altitudes from 2.75 to 4.5 km in region C in Fig. 10a, north of those in layer B. Layer D air originates in region D in Fig. 10a over far northwest Canada at 8.5–9.25-km altitude. Air arriving in layer E

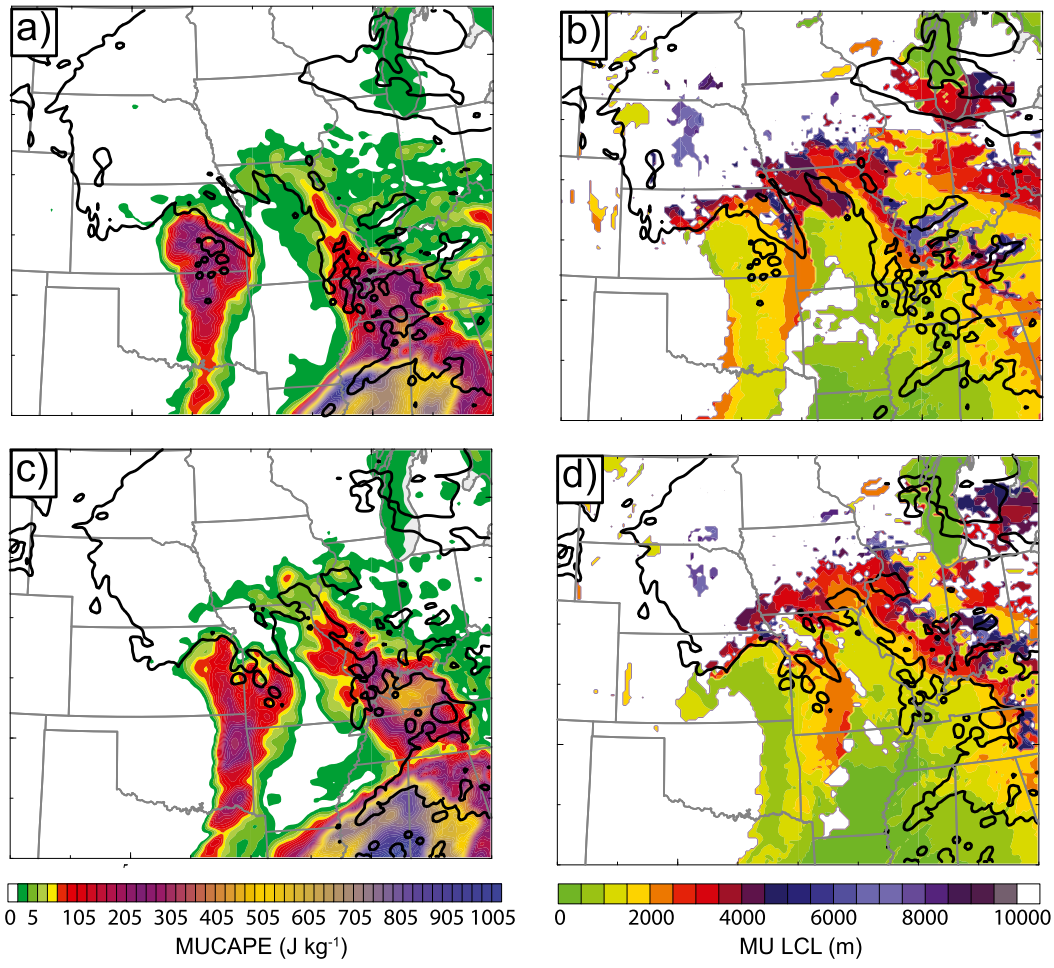

FIG. 9. (a),(c) Simulated column MUCAPE (colored) and 10-dBZ simulated reflectivity contour (black) from the WRF simulation and (b),(d) the LCL of the parcel with MUCAPE. Plots are valid at (a),(b) 0100 and (c),(d) 0300 UTC 9 Dec.

originated from region E in Fig. 10a. This region was small, so only two source points are shown on the figure. Air in layer E originated from 9.25- to 9.75-km altitude.

Overall, there was a juxtaposition of air from over the subtropical Pacific and Arctic. However, the potential instability in the comma head arose from the juxtaposition of air from two altitudes over the Pacific, west of the Baja Peninsula. In this storm, air from the Gulf of Mexico or central plains was not incorporated into the layer where the instability occurred. It is notable that air within layers A and E, the base and top of the layer in which elevated convection occurred, originated at locations up to 5000 km apart, 63 h before arriving in the same vertical cross section within the storm's comma head.

Figures 10b–d are plots of backward trajectory endpoints, as in Fig. 10a, except the panels are all for trajectories released at 0100 UTC. Figure 10b is for trajectories on the westernmost cross section in Fig. 3b, Fig. 10c is for the middle cross section, and Fig. 10d is for the easternmost cross section. The trajectories from 0100 UTC are examined because the model had fewer convective cells present at that time, so air within the potentially unstable region should be relatively undisturbed by convective overturning. All three 0100 UTC cross sections are similar to the 0300 UTC cross section, with layer A air originating near Baja California, and subsequent layers of air originating farther north and west in similar locations and altitude to the 0300 UTC cross section. The most notable difference is in Fig. 10b, the west cross section at 0100 UTC, where there was no signal of layer C, as a large, nearly neutral layer separated layers B and D (not shown).

Figure 11 shows example backward trajectories from each of the five layers released at 0300 UTC 9 December along the easternmost cross section in Fig. 3b. The

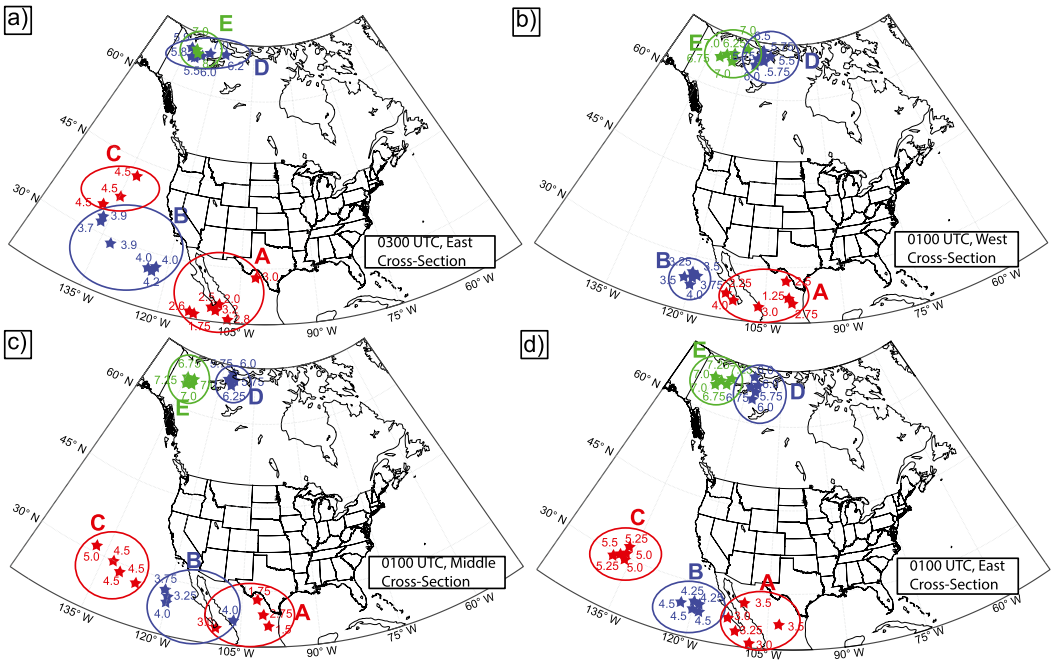

FIG. 10. Source locations for air parcels originating in each of the layers in Fig. 7; numbers indicate the altitude the backward trajectory was initialized at within the comma head. Maps are for trajectories from (a) 0300 UTC 9 Dec, easternmost cross section in Fig. 3b; (b) 0100 UTC 9 Dec, western cross section in Fig. 3b; (c) 0100 UTC 9 Dec, central cross section in Fig. 3b; and (d) 0100 UTC 9 Dec, eastern cross section in Fig. 3b.

trajectories in the left column of Fig. 11 are plan views colored by pressure, while in the right column, a time series of key parameters along with the trajectory is shown. The trajectories presented in Fig. 11 are representative of other trajectories in their respective layers. Five variables—altitude (m, blue), terrain height (m, brown), potential temperature (K, black), equivalent potential temperature (K, green), and mixing ratio ($g\,kg^{-1}$, red)—appear in Figs. 11b, 11d, 11f, 11h, and 11j. In the absence of diabatic processes, θ, θ_e, and q are conserved. These variables, along with the location of clouds and precipitation in the model and the location of terrain features, were used in determining the evolution of parcels described below.

Fig. 11a shows a trajectory from within layer A. Air arriving in layer A is the source air for the elevated convection in the comma head, as will be demonstrated in the next section. This trajectory began at hour 0 directly south of Baja California at 2250-m altitude. Air following this trajectory moved northeast, over continental Mexico, and reached the Rio Grande Valley by hour 36. At that time, the air's forward speed increased, indicated by the trajectory's arrival in north Texas at 48 h and eastern Missouri by 60 h before the air arrived at the cross section at 63 h.

The thermodynamic evolution of the layer A air appears in Fig. 11b. The air began at hour 0 around 2.3-km altitude. The air maintained roughly the same altitude until encountering higher terrain of the Sierra Madre Occidental, which forced the air to ascend over the terrain to 2.7 km at time α (Fig. 11b), where mixing with clouds and precipitation increased q by $1.5\,g\,kg^{-1}$ and θ_e by 5 K. The air then descended on the far side of the terrain at time β to around 1.5 km, mixing with cooler and drier air as q decreased $1\,g\,kg^{-1}$, and θ and θ_e each decreased by about 5 K. After this, the air slowly descended and cooled until time γ. At time γ, the air encountered clouds and precipitation behind a front located across eastern Texas, where mixing and evaporative cooling in stratiform clouds behind the front decreased θ and θ_e each by 7 K, while q increased by $1.5\,g\,kg^{-1}$. Finally, at time δ, the air ascended 1000 m within the comma head, where it precipitated out $2\,g\,kg^{-1}$ of moisture, while θ increased by 5 K and θ_e remained constant due to pseudoadiabatic ascent.

Aside from areas where air passed over mountain ranges or through clouds, both θ and θ_e steadily decreased during trajectories in Fig. 11b. This decrease, which is around 1–2 $K\,day^{-1}$, is consistent with the expected range of radiational cooling rates in the clear atmosphere (cf. Cavallo et al. 2011, their Fig. 1b). Cooling occurred along every trajectory examined, including the others presented below for higher levels. Between radiative cooling and other diabatic processes

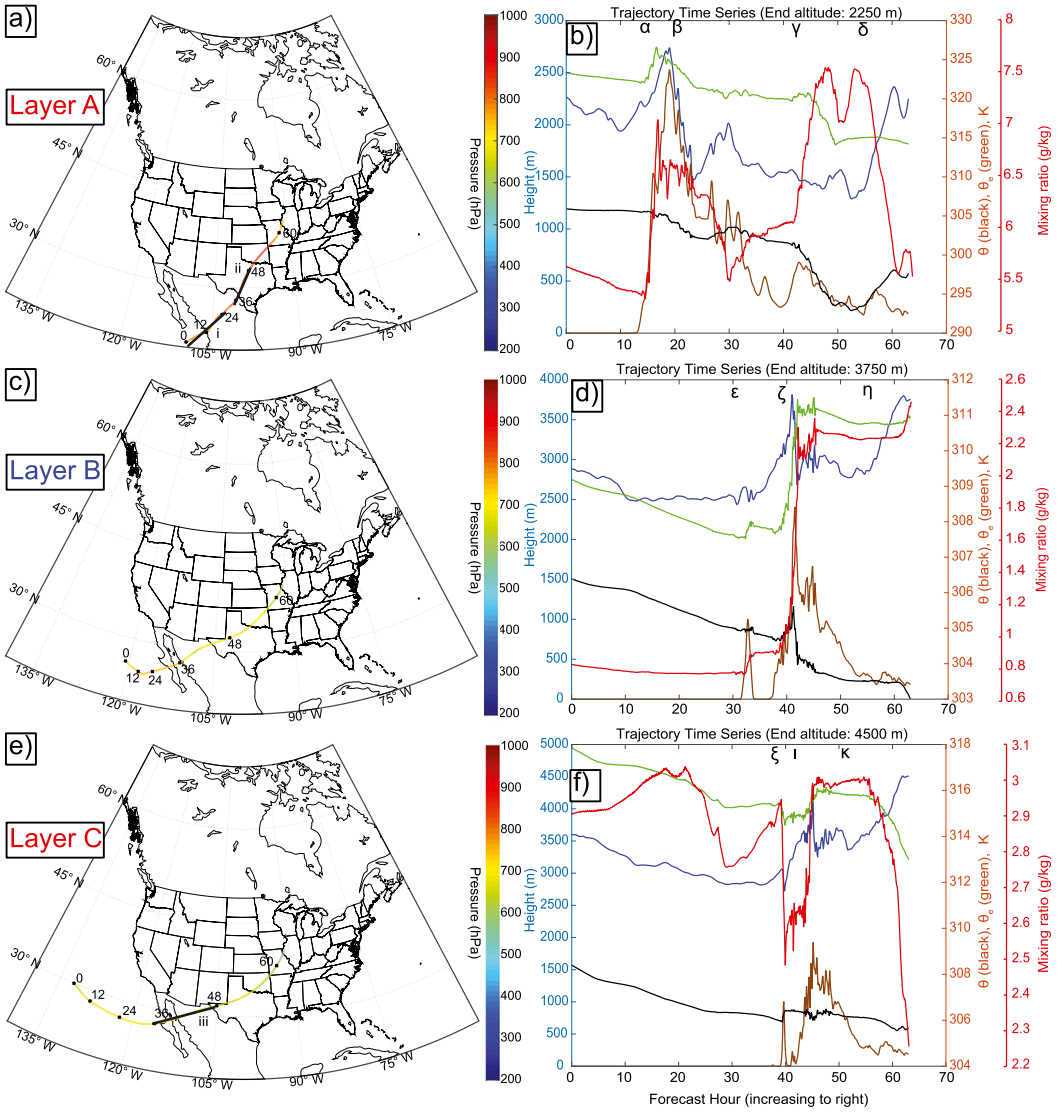

FIG. 11. Example trajectories from each of the layers in Fig. 7. Trajectories all arrive at the easternmost cross section in Fig. 3, but at different altitudes (see Fig. 7). (left) Plan view of trajectories with model forecast time indicated every 12 h. Trajectories are colored by pressure. (right) Time series of trajectory height (m, blue, left axis), height of terrain under trajectory (m, brown, left axis), equivalent potential temperature (K, green, right axis), potential temperature (K, black, right axis), and mixing ratio ($g\,kg^{-1}$, red, far right axis). Trajectories are from (a),(b) layer A; (c),(d) layer B; (e),(f) layer C; (g),(h) layer D; and (i),(j) layer E. Greek letters indicate times of interest referenced in the text. Black lines in (a),(e) indicate locations of cross sections in Fig. 12.

over the length of the trajectory in Fig. 11b, the air's θ_e value decreased from 323 to 314 K on its path to layer A. Despite this decrease, the air arrived at the cross section in layer A with a local maximum and became the source air for elevated convection.

Air arriving in layer B followed trajectories similar to the example trajectory shown in Fig. 11c. This trajectory began over the Pacific Ocean in region B in Fig. 10a, starting at 2900-m altitude, 600 m higher and 14 K lower θ_e than layer A. As with the previous trajectory, air moved across northern Mexico and accelerated after 36 h as the air entered a region of stronger flow, reaching west Texas by 48 h and central Missouri by 60 h. As shown in Fig. 11d, the air along this trajectory slowly descended from its 2900-m starting altitude and cooled diabatically at a rate consistent with radiative cooling. This diabatic cooling was evidenced by a 2 K decrease in both θ and θ_e over the first 30 h. At time ε, the air was mixed with surrounding higher-moisture air, evidenced by the 0.5 K increase in θ_e and a 0.1 $g\,kg^{-1}$ increase in q. This mixing was induced by crossing the higher terrain of Baja California. At time ζ, the air encountered the

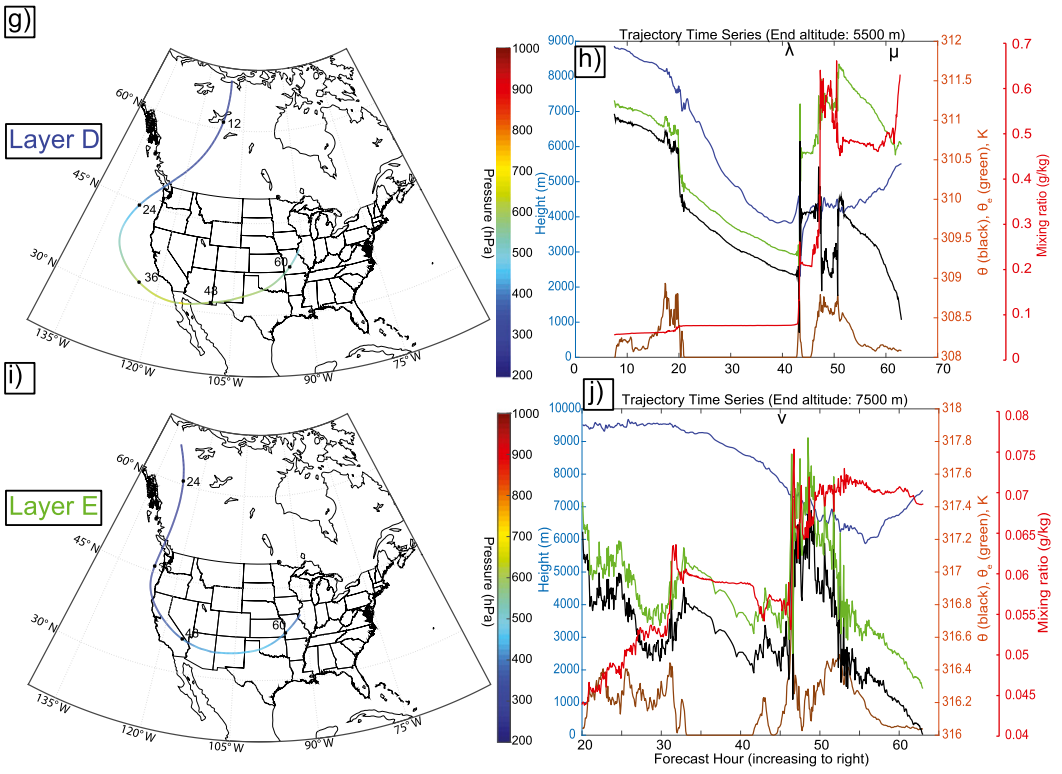

FIG. 11. (*Continued*)

Sierra Madre Occidental, which forced the air to rise 1000 m. As it rose, the air mixed with potentially warmer air, increasing θ by 1 K. The environmental air in which it mixed was associated with precipitation on the windward side of the mountains, so the air gained 4 K in θ_e as well as 1.4 g kg^{-1} in q. If θ experiences a small increase (1 K) and θ_e increases by 4 K, the only way for this to happen is for moisture and potentially warmer air to be added to the air parcel through mixing. On the other side of the mountain, θ decreased by 1 K, but θ_e held roughly steady as q increased by another 0.1 g kg^{-1}. The air then held steady in altitude until time η, where the air ascended 1000 m in the comma head region. As it did so, the conservative parameters remained essentially constant until the last hour, where the air gained 0.2 g kg^{-1} in q while θ decreased by 0.5 K due to evaporational cooling. At the end of the trajectory, the air arrived in Fig. 7b in layer B, a θ_e minimum, 4 K less than layer A.

For layer C, a secondary maximum in Fig. 7b, the source region at hour 0 was farther northwest over the Pacific Ocean than trajectories ending in layer B (Fig. 11e). Air started at 3500-m altitude, with θ_e 9 K higher than the trajectory from layer B, but the trajectory otherwise followed a similar path once it reached land, though it was moving faster owing to being farther aloft by about 500 m. Over the first 40 h, the air slowly descended 500 m and radiationally cooled (Fig. 11f), with gradual changes of 0.1–0.2 g kg^{-1} in q. There was no precipitation along the trajectory during this time period, so the slight changes in q must have been associated with mixing. At time ξ, the air moved over the higher terrain of Baja California, which caused a 0.4 g kg^{-1} decrease in q, with a 1 K increase in θ and a 1 K decrease in θ_e, all of which is likely due to mixing. At time ι, the air then moved over the Sierra Madre Occidental, which again induced mixing. This time, q increased by 0.4 g kg^{-1}, and θ_e increased by 1 K. Starting at time κ, air ascended 1000 m and mixed with drier air in the comma head, decreasing q by 0.8 g kg^{-1} while θ_e decreased by 2 K as the air arrived at the comma head. This mixing occurred due to the air ascending through a region of lower RH values aloft. At the end of the trajectory, the air arrived with a secondary θ_e maximum in layer C, 2 K higher than the trajectory in layer B below it.

A trajectory characteristic of layer D is shown in Fig. 11g. Air in this layer originated near 9-km altitude in northern Canada at model hour 8 (it was outside the model domain at hour 0) (Fig. 11h). The air in this layer moved quickly around the base of the long-wave trough (Figs. 4b,d), ending up off the coast of Oregon by 24 h, off the coast of central California by 36 h, over southeast Arizona by 48 h, and over southwest Missouri at 60 h,

arriving at the cross section in the comma head by 63 h. In Fig. 11h, the air from layer D began near 9-km altitude, and then it cooled radiationally by about 2 K (both θ and θ_e) over about 40 h as it descended by almost 5000 m. A 0.5 K decrease in theta occurred at about hour 20 due to mixing that occurred as the air crossed the Coastal Range in southwestern Canada. During this descent, q remained constant. At time λ, the air was at around 4-km altitude and moved from Baja California over the Sierra Madre Occidental, and then the Rocky Mountains. This caused the air to mix with its surroundings, which consisted of clouds and precipitation near the base of the long-wave trough. This mixing increased θ by 1 K, θ_e by 2 K, and q by 0.4 g kg^{-1}. After crossing the mountains, the air again radiationally cooled by about 1 K in θ and θ_e until time μ, when q increased by 0.2 g kg^{-1} in the last hour due to mixing/evaporational cooling in the comma head, which accelerated the decrease in θ, with less effect on θ_e.

Air from the equilibrium level (E in Fig. 7) also originated over northern Canada at 9.5-km altitude at model hour 20, west of the air from layer D (Fig. 11i). As with the previous trajectory, this air moved rapidly around the base of the long-wave trough and was located off of Oregon at 36 h, over southeastern California by 48 h, and over the Kansas–Missouri border at 60 h. From its starting altitude of 9.5 km in Fig. 11j, the air mixed over the Canadian Rockies until 32 h, after which the air cooled radiationally and slowly descended. This happened until time ν, when the air crossed over the Rocky Mountains again, causing mixing and small fluctuations in q, θ, and θ_e. After crossing the mountains, the descent stopped, and the air began to rise toward 7.5 km, with θ and θ_e again decreasing due to radiative cooling and q remaining constant.

To demonstrate diabatic changes described above, Fig. 12 shows three example cross sections along trajectories. The locations of these cross sections are indicated by the lines in Figs. 11a and 11e. Figure 12a corresponds to the environment near the trajectory's path in Fig. 11a, line i, and at forecast hour 12; this time is also close to time α in Fig. 11b. At this time, the air in the trajectory was near 2-km altitude with a potential temperature of 305 K and was approaching the Sierra Madre Occidental from the west. The air within the trajectory closely followed the 305 K isentrope as it approached the mountains. When the air reached the mountains, it encounters clouds, indicated by RH values greater than 70% in Fig. 12a. Mixing with this high-RH air produced the increased q and increased θ_e at time α in Fig. 12b. After the air traversed the high-RH environment atop the mountain, the air (now at 303 K) encountered low-RH air (<70% RH) on the leeward side of the mountain

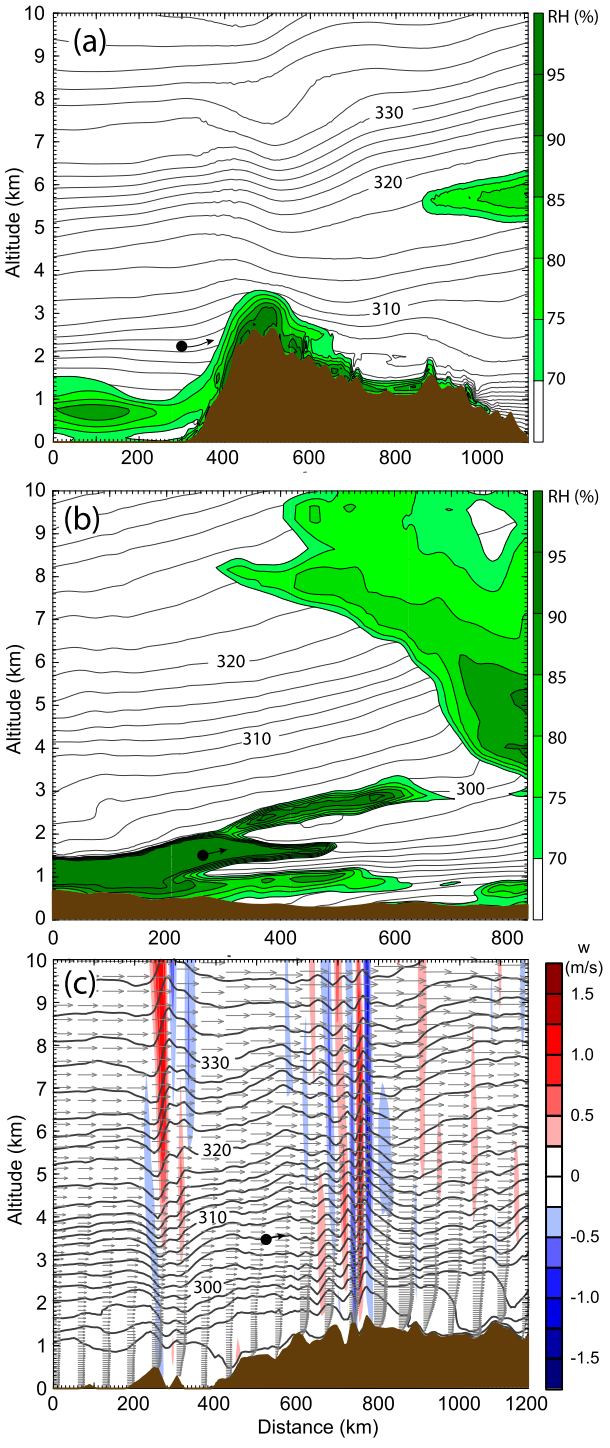

FIG. 12. Cross sections showing example times where air along trajectories in Fig. 11 underwent diabatic changes. (a),(b) Relative humidity (%) shaded and contours of potential temperature (K, contour interval 2 K). (c) Air vertical velocity (m s^{-1}) shaded, arrows indicating flow in the along-cross-sectional direction, and contours of potential temperature (K, contour interval 2 K). Circles indicate the location of the air along the trajectory at the time. (a) Valid at 1200 UTC 6 Dec (forecast hour 12) and (b),(c) valid at 0600 UTC 8 Dec (forecast hour 42) 2009.

(right side of the figure), and the air became drier at time β in Fig. 11b.

Farther along in the trajectory's path at forecast hour 42 (Fig. 11a, line *ii*), the trajectory air was within clouds and precipitation, as indicated by the high (>95%) RH environment in Fig. 12b. The trajectory air, which was located at about 1.5-km altitude and a potential temperature of ~301 K, initially experienced an increase in both q and θ_e (1 g kg^{-1} and 1 K, respectively) as seen at time γ in Fig. 11b. As the trajectory's air remained near 300 K, it exited the middle of the high-RH cloud environment (near 300 km on the x axis) and moved at the bottom of or below the shallow cloud situated between 2- and 3-km altitude. As this happened, the increase in q leveled off between 7 and 7.5 g kg^{-1}, as both θ and θ_e began to decrease as the air experienced both evaporative cooling and mixing with drier air beneath the cloud.

The cross section in Fig. 12c is an example of air aloft mixed by terrain underneath, corresponding to forecast hour 42 along the trajectory in Fig. 11e, line *iii*. At this time, the trajectory's air was located between two areas of mountain-induced vertical motions. The mountains' impact stretched up to at least 10-km altitude, well above the 3.5-km altitude of the trajectory. The small changes in q, θ, and θ_e at time ξ and time ι in Fig. 11f correspond to times when the trajectory was above the mountains and within regions of mountain-induced vertical circulations in Fig. 12c, consistent with mountain-induced turbulence, causing the diabatic changes along the trajectory at these times seen in Fig. 11f.

6. Convective cells

The trajectories in the previous section examined source air for an environment in which instability had yet to be released. In this section, the trajectories of air passing through active convective cells are examined. Several convective cells can be seen in Fig. 13, which is a cross section in the same location of Fig. 7b, but showing vertical velocity. These convective cells are on the left side of the cross section between 0 and 200 km, with vertical velocities in the cells reaching over 1 m s^{-1}.

Figure 14 shows a plan view and time series of a trajectory ending at 6.25 km at the black dot within the convective cell in Fig. 7b and Fig. 13. Air parcels at this altitude south of the convection in Fig. 13 lie in layer D and originate in northwest Canada. However, Fig. 14a shows that the air parcel arriving at point F originated near Baja California, the origin for parcels in layer A. Like layer A in Fig. 11a, air from this convective cell moved northeast over Mexico, Texas, Oklahoma, and

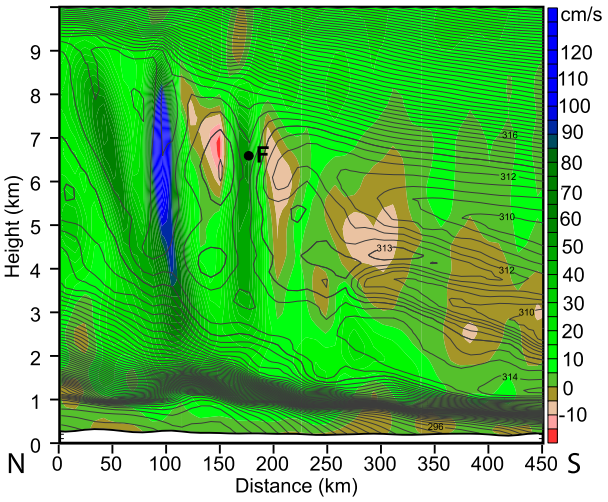

FIG. 13. Simulated vertical velocity (colors, cm s^{-1}) and equivalent potential temperature (contours, 0.5 K) valid at 0300 UTC 9 Dec 2009. Black dot is point F, the release point for the trajectory in Fig. 14.

Missouri before arriving at the cross section (Fig. 14a). In Fig. 14b, the evolution of the parcel is similar to the evolution of the layer A air in Fig. 11b, with the air starting out at around 2500 m. At time ξ in Fig. 14b, the air began to cross the Sierra Madre Occidental and encountered the same windward clouds and precipitation as air from layer A did, which here caused a 3 K increase in θ_e, a 1.5 g kg^{-1} increase in q, and a 2 K decrease in θ. On the other side of the mountains, air cooled radiatively until time o, where the air encountered postfrontal precipitation, which induced evaporative cooling, including a 0.5 K increase in θ_e, a 1 g kg^{-1} increase in q, and a 2 K decrease in θ by hour 40. After that, having descended only 500 m through time σ, the air began to rise into the comma head region, mixing with the saturated air aloft, increasing θ by 3 K, θ_e by 2 K, and q by 1 g kg^{-1}. At this point, the air begins to rise rapidly as convection through the potentially unstable layer at time τ, gaining 3000-m altitude in under an hour and rapidly losing moisture due to precipitation during pseudoadiabatic ascent, as q decreased by 3.5 g kg^{-1}. Because the ascent is pseudoadiabatic, θ increases by 4 K, but θ_e remained essentially unchanged. Trajectories in other convective cells showed similar behavior.

7. Discussion

The trajectory analyses in sections 5 and 6 reveal that the production of instability in the comma head region is not a simple, straightforward process. The analyses show that potential instability, at least in this cyclone, formed by the vertical arrangement of air from sources up to

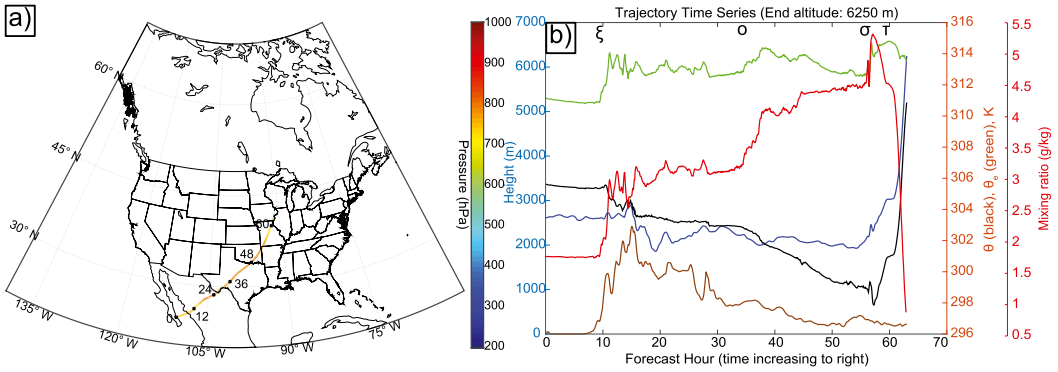

FIG. 14. As in Fig. 11, but for a backward trajectory within the convective cell released at point F in Figs. 7 and 13.

5000 km apart, with the base of the potentially unstable layer sourced near Baja California or over continental Mexico and the air at the equilibrium layer sourced in the Arctic. The layer in which convection occurred itself consisted of five distinct layers, with each layer being sourced from distinct locations. Notably absent was any air from the Gulf of Mexico region. Air from over the Gulf was confined to the low-level stable layer. The potentially unstable layer comprised air sourced over or near the Pacific Ocean near and north of Baja California.

As the air approached the cyclone and formed the comma head, it underwent a number of diabatic changes due to mixing, condensation, evaporation, and radiational cooling. The magnitude of these changes implies that the upstream parcel initial thermodynamic properties do not necessarily represent or predict the final thermodynamic state due to the diabatic changes occurring along the trajectories. Trajectory A started with θ_e 14 K higher than trajectory B, but by 63 h, the θ_e difference was reduced to 3 K. Diabatic changes were found to occur all along the trajectories due to radiational cooling, which was 1–2 K day^{-1}. The implication is that the air never truly moved in an isentropic framework, even over short time scales. Aside from radiative cooling, there were also diabatic changes along trajectories due to terrain influences. Since the air in the layer where convection occurred was sourced over the Pacific or northwestern Canada, any path to the midwestern United States had to cross mountain ranges, such as the Rocky Mountains or the Sierra Madre Occidental. The data along the trajectory paths showed that as the air crossed these mountains, fluctuations of 1–3 K (in some cases, 5 K or more) occurred in θ and θ_e as the air was forced to rise, encountered turbulence above the mountains, mixed with other air, and/or passed through orographic clouds. Terrain effects were evident throughout the depth of the troposphere, though trajectories at higher altitudes (those from layer E) were only minimally affected, with fluctuations in θ and θ_e generally less than 1 K. These processes are complicated and seemingly unrelated; however, in aggregate, the along-trajectory diabatic changes combine to produce elevated instability.

The simulated cyclone had a broad region of elevated instability in the comma head, and trajectories from across the region where convection developed in the model indicated that the instability developed in a similar way. The model results show that the generation of instability in the comma head region is an ongoing process as airstreams approach and arrive within the comma head from different source regions. Thermodynamic properties of the air are continuously altered by diabatic processes as the air approaches and passes into the storm. Because of this, any relationship between parcel initial properties and instability is not obvious from this one case. Further similar analyses of other cyclones are necessary to examine any possible relationship between parcel properties and final instability magnitudes.

8. Conclusions

A 63-h Weather Research and Forecasting Model simulation was carried out to quantify and understand the development of elevated convection in the comma head region of a strong continental winter cyclone. The presence of elevated potential instability in the model was demonstrated and was compared favorably with observations of the actual cyclone. The favorable comparison provided confidence that the simulation could be used to demonstrate how the environment for elevated convection forms.

The significant findings of this work are as follows:

1) The layer where convection occurred within the comma head region consisted of air from geographically diverse

source regions, ranging from Baja California to the Arctic. From this one case study, it is not clear if particular source regions are important to the development of potential instability.

2) Air from over and near the Pacific Ocean was important in the generation of potential instability in this cyclone, as almost all of the trajectories within the unstable layer were sourced from there 60 h earlier.
3) Air from the Gulf of Mexico was not involved in the generation of elevated convection in the cyclone's comma head and was confined under the stable layer.
4) The elevated convectively unstable region of the comma head consisted of five layers between the level of free convection (LFC; layer A) and the equilibrium level (EL; layer E). Air within each layer was sourced from similar geographic regions. The layers were characterized by maxima or minima of θ_e. The layers in which the instability developed sourced from altitudes in the lower and midtroposphere. Studies of storms in Britain show tropopause folding to be important to the development of convection within the warm conveyor belt of winter cyclones. The trajectory analyses for this storm illustrate a different mechanism for the development of elevated convection.
5) Air along trajectories was found to undergo constant diabatic change. This usually took the form of radiational cooling, but also included mixing during passage over mountains and heating or cooling during passage through clouds and precipitation. Diabatic changes have been noted to be important in previous trajectory studies of snowstorms along the U.S. East Coast (Fuhrmann and Konrad 2013). In both the Fuhrmann and Konrad (2013) paper and in this paper, the initial thermodynamic properties of air were not predictive of the properties of the air in the comma head based on application of isentropic flow.
6) When backward trajectories were calculated from within elevated convective cells, the trajectories captured the ascent of air from the LFC to the EL, showing that the air within convective cells and environmental air at the LFC were sourced from the same location.

The results presented here are from one storm, a deep cyclone that produced over 30–40 cm (12–16 in.) of snow beneath the comma head. Based on evidence of wintertime lightning in the comma head presented by Market et al. (2006), Rauber et al. (2014), and Warner et al. (2014), it is likely that processes creating elevated potential instability described herein also occur within the comma head of other strong continental cyclones. However, more research is required to show whether the findings of this study can be generalized.

Acknowledgments. This work was funded under National Science Foundation Grants ATM-0833828 and AGS-1247404. Additional funding was provided by NOAA/Office of Oceanic and Atmospheric Research under NOAA–University of Oklahoma Cooperative Agreement NA11OAR4320072, U.S. Department of Commerce. The authors acknowledge the Texas Advanced Computing Center (TACC) at The University of Texas at Austin for providing HPC resources that have contributed to the research results reported within this paper. These computing resources were provided under XSEDE Award TG-ATM050014N. The composite radar analysis appearing in Figs. 3a and 6a was provided by the Iowa Environmental Mesonet, maintained by the Iowa State University Department of Agronomy. RUC data were provided by the National Climatic Data Center. The authors thank the three anonymous reviewers, whose suggestions improved this manuscript.

REFERENCES

Benjamin, S. G., and Coauthors, 2004: An hourly assimilation–forecast cycle: The RUC. *Mon. Wea. Rev.*, **132**, 495–518, https://doi.org/10.1175/1520-0493(2004)132<0495:AHACTR>2.0.CO;2.

Browning, K. A., and B. W. Golding, 1995: Mesoscale aspects of a dry intrusion within a vigorous cyclone. *Quart. J. Roy. Meteor. Soc.*, **121**, 463–493, https://doi.org/10.1002/qj.49712152302.

Cavallo, S. M., J. Dudhia, and C. Snyder, 2011: A multilayer upper-boundary condition for longwave radiative flux to correct temperature biases in a mesoscale model. *Mon. Wea. Rev.*, **139**, 1952–1959, https://doi.org/10.1175/2010MWR3513.1.

Colman, B. R., 1990: Thunderstorms above frontal surfaces in environments without positive CAPE. Part I: A climatology. *Mon. Wea. Rev.*, **118**, 1103–1122, https://doi.org/10.1175/1520-0493(1990)118<1103:TAFSIE>2.0.CO;2.

Curran, J. T., and A. D. Pearson, 1971: Proximity soundings for thunderstorms with snow. Preprints, *Seventh Conf. on Severe Local Storms,* Kansas City, MO, Amer. Meteor. Soc., 118–119.

Fuhrmann, C. M., and C. E. Konrad II, 2013: A trajectory approach to analyzing the ingredients associated with heavy winter storms in central North Carolina. *Wea. Forecasting*, **28**, 647–667, https://doi.org/10.1175/WAF-D-12-00079.1.

Griffiths, M., A. J. Thorpe, and K. A. Browning, 2000: Convective destabilization by a tropopause fold diagnosed using potential-vorticity inversion. *Quart. J. Roy. Meteor. Soc.*, **126**, 125–144, https://doi.org/10.1002/qj.49712656207.

Grim, J. A., R. M. Rauber, M. K. Ramamurthy, B. F. Jewett, and M. Han, 2007: High- resolution observations of the trowal–warm-frontal region of two continental winter cyclones. *Mon. Wea. Rev.*, **135**, 1629–1646, https://doi.org/10.1175/MWR3378.1.

Halcomb, C. E., and P. S. Market, 2003: Forcing, instability and equivalent potential vorticity in a Midwest USA convective snowstorm. *Meteor. Appl.*, **10**, 273–280, https://doi.org/10.1017/S1350482703003074.

Han, M., R. M. Rauber, M. K. Ramamurthy, B. F. Jewett, and J. A. Grim, 2007: Mesoscale dynamics of the trowal and warm-frontal regions of two continental winter cyclones. *Mon. Wea. Rev.*, **135**, 1647–1670, https://doi.org/10.1175/MWR3377.1.

Holle, R. L., and J. V. Cortinas Jr., 1998: Thunderstorms observed at surface temperatures near and below freezing across North America. Preprints, *19th Conf. on Severe Local Storms,* Minneapolis, MN, Amer. Meteor. Soc., 705–708.

Iacono, M. J., E. J. Mlawer, S. A. Clough, and J. Morcrette, 2000: Impact of an improved longwave radiation model, RRTM, on the energy budget and thermodynamic properties of the NCAR community climate model, CCM3. *J. Geophys. Res.*, **105**, 14 873–14 890, https://doi.org/10.1029/2000JD900091.

Kain, J. S., and J. M. Fritsch, 1990: A one-dimensional entraining/detraining plume model and its application in convective parameterization. *J. Atmos. Sci.*, **47**, 2784–2802, https://doi.org/10.1175/1520-0469(1990)047<2784:AODEPM>2.0.CO;2.

Keeler, J. M., B. F. Jewett, R. M. Rauber, G. M. McFarquhar, R. M. Rasmussen, L. Xue, C. Liu, and G. Thompson, 2016a: Dynamics of cloud-top generating cells in winter cyclones. Part I: Idealized simulations in the context of field observations. *J. Atmos. Sci.*, **73**, 1507–1527, https://doi.org/10.1175/JAS-D-15-0126.1.

——, ——, ——, ——, ——, ——, ——, and ——, 2016b: Dynamics of cloud-top generating cells in winter cyclones. Part II: Radiative and instability forcing. *J. Atmos. Sci.*, **73**, 1529–1553, https://doi.org/10.1175/JAS-D-15-0127.1.

——, R. M. Rauber, B. F. Jewett, G. M. McFarquhar, R. M. Rasmussen, L. Xue, C. Liu, and G. Thompson, 2017: Dynamics of cloud-top generating cells in winter cyclones. Part III: Shear and convective organization. *J. Atmos. Sci.*, **74**, 2879–2897, https://doi.org/10.1175/JAS-D-16-0314.1.

Klemp, J. B., J. Dudhia, and A. D. Hassiotis, 2008: An upper gravity-wave absorbing layer for NWP applications. *Mon. Wea. Rev.*, **136**, 3987–4004, https://doi.org/10.1175/2008MWR2596.1.

Kumjian, M. R., S. A. Rutledge, R. M. Rasmussen, P. C. Kennedy, and M. Dixon, 2014: High-resolution polarimetric radar observations of snow-generating cells. *J. Appl. Meteor. Climatol.*, **53**, 1636–1658, https://doi.org/10.1175/JAMC-D-13-0312.1.

Market, P. S., C. E. Halcomb, and R. L. Ebert, 2002: A climatology of thundersnow events over the contiguous United States. *Wea. Forecasting*, **17**, 1290–1295, https://doi.org/10.1175/1520-0434(2002)017<1290:ACOTEO>2.0.CO;2.

——, and Coauthors, 2006: Proximity soundings of thundersnow in the central United States. *J. Geophys. Res.*, **111**, D19208, https://doi.org/10.1029/2006JD007061.

Martin, J. E., 1998: The structure and evolution of a continental winter cyclone. Part II: Frontal forcing of an extreme snow event. *Mon. Wea. Rev.*, **126**, 329–348, https://doi.org/10.1175/1520-0493(1998)126<0329:TSAEOA>2.0.CO;2.

Moore, J. T., C. E. Graves, S. Ng, and J. L. Smith, 2005: A process-oriented methodology toward understanding the organization of an extensive mesoscale snowband: A diagnostic case study of 4–5 December 1999. *Wea. Forecasting*, **20**, 35–50, https://doi.org/10.1175/WAF-829.1.

Murphy, A. M., R. M. Rauber, G. M. McFarquhar, J. A. Finlon, D. M. Plummer, A. A. Rosenow, and B. F. Jewett, 2017: A microphysical analysis of elevated convection in the comma head region of continental winter cyclones. *J. Atmos. Sci.*, **74**, 69–91, https://doi.org/10.1175/JAS-D-16-0204.1.

Nicosia, D. J., and R. H. Grumm, 1999: Mesoscale band formation in three major northeastern United States snowstorms. *Wea. Forecasting*, **14**, 346–368, https://doi.org/10.1175/1520-0434(1999)014<0346:MBFITM>2.0.CO;2.

Novak, D. R., B. A. Colle, and S. E. Yuter, 2008: High-resolution observations and model simulations of the life cycle of an intense mesoscale snowband over the northeastern United States. *Mon. Wea. Rev.*, **136**, 1433–1456, https://doi.org/10.1175/2007MWR2233.1.

——, ——, and R. McTaggart-Cowan, 2009: The role of moist processes in the formation and evolution of mesoscale snowbands within the comma head of northeast U.S. cyclones. *Mon. Wea. Rev.*, **137**, 2662–2686, https://doi.org/10.1175/2009MWR2874.1.

——, ——, and A. R. Aiyyer, 2010: Evolution of mesoscale precipitation band environments within the comma head of northeast U.S. cyclones. *Mon. Wea. Rev.*, **138**, 2354–2374, https://doi.org/10.1175/2010MWR3219.1.

Pfahl, S., E. Madonna, M. Boettcher, H. Joos, and H. Wernli, 2014: Warm conveyor belts in the ERA-Interim data set (1979–2010). Part II: Moisture origin and relevance for precipitation. *J. Climate*, **27**, 27–40, https://doi.org/10.1175/JCLI-D-13-00223.1.

Plummer, D. M., G. M. McFarquhar, R. M. Rauber, B. F. Jewett, and D. C. Leon, 2014: Structure and statistical analysis of the microphysical properties of generating cells in the comma head region of continental winter cyclones. *J. Atmos. Sci.*, **71**, 4181–4203, https://doi.org/10.1175/JAS-D-14-0100.1.

——, ——, ——, ——, and ——, 2015: Microphysical properties of convectively generated fall streaks within the stratiform comma head region of continental winter cyclones. *J. Atmos. Sci.*, **72**, 2465–2483, https://doi.org/10.1175/JAS-D-14-0354.1.

Rasp, S., T. Selz, and G. C. Craig, 2016: Convective and slantwise trajectory ascent in convection-permitting simulations of midlatitude cyclones. *Mon. Wea. Rev.*, **144**, 3961–3976, https://doi.org/10.1175/MWR-D-16-0112.1.

Rauber, R. M., and Coauthors, 2014: Stability and charging characteristics of the comma head region of continental winter cyclones. *J. Atmos. Sci.*, **71**, 1559–1582, https://doi.org/10.1175/JAS-D-13-0253.1.

——, and Coauthors, 2015: The role of cloud-top generating cells and boundary layer circulations in the finescale radar structure of a winter cyclone over the Great Lakes. *Mon. Wea. Rev.*, **143**, 2291–2318, https://doi.org/10.1175/MWR-D-14-00350.1.

Reed, R. J., 1955: A study of a characteristic type of upper-level frontogenesis. *J. Meteor.*, **12**, 226–237, https://doi.org/10.1175/1520-0469(1955)012<0226:ASOACT>2.0.CO;2.

——, and F. Sanders, 1953: An investigation of the development of a mid-tropospheric frontal zone and its associated vorticity field. *J. Meteor.*, **10**, 338–349, https://doi.org/10.1175/1520-0469(1953)010<0338:AIOTDO>2.0.CO;2.

Rosenow, A. R., D. M. Plummer, R. M. Rauber, G. M. McFarquhar, B. F. Jewett, and D. Leon, 2014: Vertical velocity and physical structure of generating cells and convection in the comma head region of continental winter cyclones. *J. Atmos. Sci.*, **71**, 1538–1558, https://doi.org/10.1175/JAS-D-13-0249.1.

Schultz, D. M., and C. F. Mass, 1993: The occlusion process in a midlatitude cyclone over land. *Mon. Wea. Rev.*, **121**, 918–940, https://doi.org/10.1175/1520-0493(1993)121<0918:TOPIAM>2.0.CO;2.

——, and P. N. Schumacher, 1999: The use and misuse of conditional symmetric instability. *Mon. Wea. Rev.*, **127**, 2709–2732, https://doi.org/10.1175/1520-0493(1999)127<2709:TUAMOC>2.0.CO;2.

Schumacher, R. S., and R. H. Johnson, 2008: Mesoscale processes contributing to extreme rainfall in a midlatitude warm-season flash flood. *Mon. Wea. Rev.*, **136**, 3964–3986, https://doi.org/10.1175/2008MWR2471.1.

Sippel, J. A., S. A. Braun, and C. Shie, 2011: Environmental influences on the strength of Tropical Storm Debby (2006). *J. Atmos. Sci.*, **68**, 2557–2581, https://doi.org/10.1175/2011JAS3648.1.

Skamarock, W. C., and Coauthors, 2008: A description of the Advanced Research WRF version 3. NCAR Tech. Note NCAR/TN-475+STR, 113 pp., https://doi.org/10.5065/D68S4MVH.

Stoelinga, M. T., 2009: A users' guide to RIP version 4.5: A program for visualizing mesoscale model output. University of Washington, accessed 28 September 2017, http://www2.mmm.ucar.edu/wrf/users/docs/ripug.htm.

Thompson, G., P. R. Field, R. M. Rasmussen, and W. D. Hall, 2008: Explicit forecasts of winter precipitation using an improved bulk microphysics scheme. Part II: Implementation of a new snow parameterization. *Mon. Wea. Rev.*, **136**, 5095–5115, https://doi.org/10.1175/2008MWR2387.1.

Warner, T. A., T. J. Lang, and W. A. Lyons, 2014: Synoptic scale outbreak of self-initiated upward lightning (SIUL) from tall structures during the central U.S. blizzard of 1–2 February 2011. *J. Geophys. Res. Atmos.*, **119**, 9530–9548, https://doi.org/10.1002/2014JD021691.

Wernli, B. H., and H. C. Davies, 1997: A Lagrangian-based analysis of extratropical cyclones. I: The method and some applications. *Quart. J. Roy. Meteor. Soc.*, **123**, 467–489, https://doi.org/10.1002/qj.49712353811.

Wexler, R., and D. Atlas, 1959: Precipitation generating cells. *J. Meteor.*, **16**, 327–332, https://doi.org/10.1175/1520-0469(1959)016<0327:PGC>2.0.CO;2.

Wiesmueller, J. L., and S. M. Zubrick, 1998: Evaluation and application of conditional symmetric instability, equivalent potential vorticity, and frontogenetic forcing in an operational forecast environment. *Wea. Forecasting*, **13**, 84–101, https://doi.org/10.1175/1520-0434(1998)013<0084:EAAOCS>2.0.CO;2.